

Approaching phase-imaging through defocusing shadowgraphy for acoustic resonator diagnosis and the capability of direct index-of-refraction measurements

Cite as: Rev. Sci. Instrum. **92**, 103703 (2021); <https://doi.org/10.1063/5.0058334>

Submitted: 22 June 2021 • Accepted: 18 September 2021 • Published Online: 07 October 2021

 Yi You and  Jens Riedel



View Online



Export Citation



CrossMark

ARTICLES YOU MAY BE INTERESTED IN

[Design and implementation of DC-to-DC converter topology for current regulated lightning generator](#)



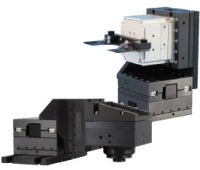
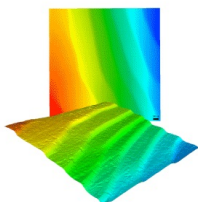
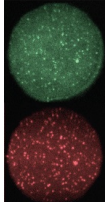
Review of Scientific Instruments **92**, 104709 (2021); <https://doi.org/10.1063/5.0060247>

[Design of a tunable turnstile mode converter for high-power microwave applications](#)

Review of Scientific Instruments **92**, 104708 (2021); <https://doi.org/10.1063/5.0046613>

[Relative calibration of a retarding field energy analyzer sensor array for spatially resolved measurements of the ion flux and ion energy in low temperature plasmas](#)

Review of Scientific Instruments **92**, 103503 (2021); <https://doi.org/10.1063/5.0059658>

 MCL MAD CITY LABS INC. www.madcitylabs.com	<p>Nanopositioning Systems</p> 	<p>Modular Motion Control</p> 	<p>AFM and NSOM Instruments</p> 	<p>Single Molecule Microscopes</p> 
---	--	--	---	--

Approaching phase-imaging through defocusing shadowgraphy for acoustic resonator diagnosis and the capability of direct index-of-refraction measurements

Cite as: Rev. Sci. Instrum. 92, 103703 (2021); doi: 10.1063/5.0058334

Submitted: 22 June 2021 • Accepted: 18 September 2021 •

Published Online: 7 October 2021



View Online



Export Citation



CrossMark

Yi You^{a1}  and Jens Riedel 

AFFILIATIONS

Federal Institute for Materials Research and Testing (BAM), Berlin D-12489, Germany

^{a1} Author to whom correspondence should be addressed: yi.you@bam.de

ABSTRACT

The visualization of index-of-refraction (IoR) distribution is one of the common methods to investigate fluid flow or pressure fields. While schlieren and shadowgraphy imaging techniques are widely accepted, their inherent limitations often lead to difficulties in elucidating the IoR distribution and extracting the true IoR information from the resulting images. While sophisticated solutions exist, the IoR-gradient-to-image was achieved by purposely introducing a commonly avoided “defect” into the optical path of a conventional coincident schlieren/shadowgraphy setup; the defect is a combination of slight defocusing and the use of non-conjugate optical components. As such, the method presented in this work is referred to as defocusing shadowgraphy, or DF-shadowgraphy. While retaining the ease of a conventional schlieren/shadowgraphy geometry, this DF approach allows direct visualization of complicated resonant acoustic fields even without any data processing. For instance, the transient acoustic fields of a common linear acoustic resonator and a two-dimensional one were directly visualized without inversion. Moreover, the optical process involved in DF-shadowgraphy was investigated from a theoretical perspective. A numerical solution of the sophisticated impulse response function was obtained, which converts the phase distortion into intensity distributions. Based on this solution, the IoRs of various gas streams (e.g., CO₂ and isopropanol vapor) were determined from single images.

© 2021 Author(s). All article content, except where otherwise noted, is licensed under a Creative Commons Attribution (CC BY) license (<http://creativecommons.org/licenses/by/4.0/>). <https://doi.org/10.1063/5.0058334>

INTRODUCTION

For flow visualizations, schlieren imaging and shadowgraphy have been greatly used as a convenient toolset for more than a century, both of which convert the optical perturbations caused by inhomogeneities in the index-of-refraction (IoR) distribution into images.^{1–3} While shadowgraphy is commonly used in cases where the IoR changes are localized and significant, e.g., shockwaves, schlieren imaging techniques are preferred for fluid-dynamic-related studies because of their high sensitivity. Recently, background-oriented schlieren techniques have overtaken conventional back-illumination methods, which is especially true for large objects.^{4,5} However, for small-scale laboratory studies, the back-illumination infrastructure is still of great interest because of its

simplicity. One of the most commonly reported flow visualization methods capable of detecting minor changes in the IoR is achieved by placing the edge of a razor blade at the focal point near the camera objective.²

While generating schlieren images through knife edges became popular in the scientific community and among hobbyists, the inherent limitations of such approaches are well known. One major drawback is that the schlieren sensitivity only occurs along the direction perpendicular to the blade edge; this issue commonly requires careful alignment of the target object to maximize spatial features in the final images. Meanwhile, the resulting image of a knife-edge schlieren system nearly shows the first-order derivative of the refractive gradient in the target region. Consequently, zero changes are expected at the maxima of an IoR gradient, leading to

counterintuitive results. Despite the future difficulties in IoR gradient reconstructions and quantitative measurements,^{3,6-8} the limitations listed above severely restrain the use of convenient schlieren methods for visualizing complex structures. In a sense that the spatial information should be preserved in all directions and maximal values are observed directly corresponding to the true distribution, shadowgraphic techniques are superior to schlieren methods. However, the governing principle of shadowgraphic image formation, the second-order derivative of an IoR gradient, concluded the low-sensitivity nature of shadowgraphy.¹

One of the demanding fields for rapid and simple visualization is related to ultrasonic resonators,⁹ e.g., ultrasonic levitation. The capability of non-contact object handling in the open air through ultrasonic levitators is greatly favored by many aspects such as performing chemical reactions,^{10,11} crystallization,^{12,13} and sample introductions,^{14,15} as optical resonance cavities,¹⁶ etc. All of the emerging needs of flexible ultrasonic levitators enabled the development of ultrasonic resonators that are more sophisticated than the common one-dimensional traps,^{17,18} which consist of a pair of a transducer and a reflector.¹⁹ However, the complexity in characterizing the acoustic fields increases as the geometry of an ultrasonic resonator gets complicated. Practically, acoustic field visualizations are often achieved by expensive laser Doppler vibrometers,²⁰ time-consuming raster scanning with probe-microphones,^{20,21} or merely through idealized mathematical simulations.^{22,23} It would be a “best of both worlds” scenario to optically “observe” an acoustic field in real-time through a platform that is as simple and sensitive as schlieren imaging with a quantifiable and anisotropic response along all directions as shadowgraphy.

From an imaging perspective, the sampling objects should ideally be sharply focused; this concept also applies to either shadowgraphic or schlieren imaging. Despite the chromatic and spherical aberrations, the blurriness due to defocusing is usually avoided intentionally. However, a few reports along with this present work suggest that slight defocusing of the images (or focused on a virtual plane) on a shadowgraphic setup reveals weaker patterns/features of an IoR gradient^{24,25} at the cost of minor image blurriness. Moreover, the optical transfer function or the impulse response function becomes a complex one. Inversions from a defocused image to a sharp one while resolving the spatial information carried by the image are complicated, even though more sophisticated imaging techniques exist, e.g., lensless imaging.²⁶ Due to the contradictions between the simple optical geometry of shadowgraphy and the

excessive complications involved in a resulting image, optical investigations of IoR gradients through shadowgraphy with deliberate defocusing were rarely reported.

In the present work, we explore the information hidden inside deliberately defocused shadowgraphic images based on a simple single-mirror coincident optical geometry to characterize gas-phase IoR gradients. In the context of “defocusing shadowgraphy (DF-shadowgraphy),” these terms are referred to as on-purpose defocusing and are based on a shadowgraphic geometry. The method introduced in this work should not be confused with the method termed “defocusing volumetric shadowgraphy.”^{27,28} To demonstrate the capability of DF-shadowgraphy (termed DF-shadowgraphy throughout this work), a set of experiments, including gas-stream imaging, and mapping of acoustic pressure fields are presented in this work as model samples. Specifically, we choose a commonly used one-dimensional ultrasonic resonator to illustrate the potential of DF-shadowgraphy in terms of force analyses for object handling.^{20,29} Moreover, a two-dimensional ultrasonic resonator that consists of four transducers was used as a model example to demonstrate the use of DF-shadowgraphy for imaging complicated spatial IoR patterns induced by superimposed interfering acoustic waves. The agreement between experimentally determined acoustic fields and numerical simulations supported the validity of the DF-shadowgraphy method. Furthermore, the imaging of IoR gradients due to defocusing is explored through a Fourier-optics theoretical framework,³⁰ implying that DF-shadowgraphy possesses the capability of determining the absolute IoR distribution from a single image.

INITIAL EVALUATION OF DF-SHADOWGRAPHY

To gain a first glance at DF-shadowgraphy, we used one of the most common optical geometries, i.e. the coincident single-mirror system [Fig. 1(a)], to obtain the knife-edge schlieren and DF-shadowgraphy images. Because schlieren imaging and shadowgraphy are closely related to each other, this shared platform provided a direct comparison between them. To switch from the schlieren geometry to that of DF-shadowgraphy, the spatial filter (i.e. the knife-edge) was removed, and the focusing objective [Fig. 1(a), focusing lens (FL)] was moved downstream to the direction of light (toward the camera) by 2.0 mm, or $d = 2.0$ mm, from the point at which the image was at focus. In this way, e.g., the pumped air stream carrying isopropanol vapor ejected from a 1/16-in.

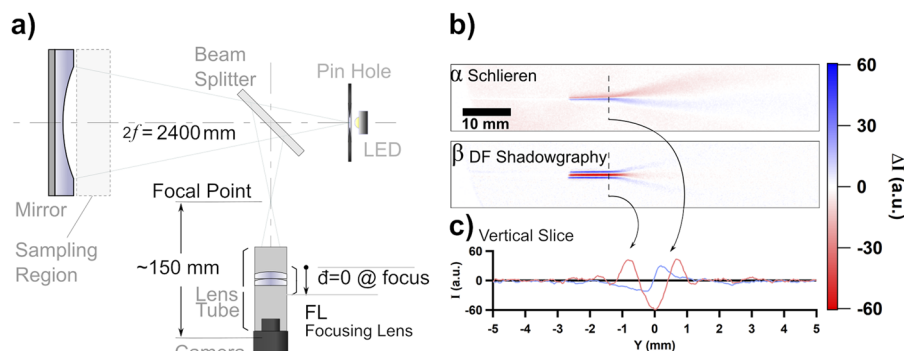


FIG. 1. Single-mirror coincident geometry (a) and the comparison between knife-edge schlieren imaging (b- α) and defocusing (DF) shadowgraphy (b- β). Vertical slices of both images at the dashed line marked in (b) are provided in (c), where the red and blue solid traces represent DF-shadowgraphy and knife-edge schlieren imaging, respectively.

outer-diameter stainless tube (supplementary material, Sec. 1, Fig. S1) was visualized through both methods. Experimentally, signal and background images were recorded with and without the gas stream, respectively. For both knife-edge schlieren and DF-shadowgraphic imaging, background-subtracted images were obtained [Figs. 1(b- α) and 1(b- β)]. The images without background subtractions can be found in the supplementary material [Figs. S6(a) and S6(c)]. The knife-edge schlieren image [Fig. 1(b- α)] showed a typical pattern close to the first-order derivative of the IoR gradient. The DF-shadowgraphy image resembled the near second-order derivative of the IoR gradient [Fig. 1(b- β)].

Based on these images, the sensitivities of knife-edge schlieren and DF-shadowgraphic imaging can be conceptually compared. Here, the absolute pixel-intensity change due to the presence of a gas stream was used as a benchmark. Vertical slices at ~ 9 mm after the gas outlet of both knife-edge schlieren and DF-shadowgraphy are shown for a direct comparison [Fig. 1(c) blue and red traces, respectively]. Semi-quantitatively, such results suggest that defocusing shadowgraphy can be more sensitive than knife-edge schlieren imaging. Moreover, the mathematical relationship between the first- and second-order derivatives indicated that the direction of moving the focusing lens toward the camera (i.e. $d > 0$) yielded the same sign of change in the refractive index as an upward-pointing knife-edge in the schlieren setup.

When moving further away from the gas outlet beyond 9 mm, the sensitivity response gets inverted. Specifically, the sensitivity of DF-shadowgraphy is higher than that of knife-edge schlieren close to the outlet capillary and vice versa. This important non-linear sensitivity of DF-shadowgraphy will be further discussed in a later part of this work. Nonetheless, the sensitivity of DF-shadowgraphy can be summarized to be competitive to traditional schlieren methods. To demonstrate the advantages of DF-shadowgraphy for 2D imaging applications, the gas-stream direction was set perpendicular to the knife-edge, clearly demonstrating that DF-shadowgraphy does not suffer from the inherent limitations of direction-related sensitivity as knife-edge schlieren imaging [Figs. S6(e) and S6(f)]. The simple evaluation of DF-shadowgraphy with a gas stream indicates the possible use of this method as an alternative to knife-edge schlieren imaging.

VISUALIZATION OF A ONE-DIMENSIONAL ACOUSTIC RESONATOR

Based on the initial investigations of DF-shadowgraphy, it is possible to implement this method toward more sophisticated objects such as resonant acoustic fields. A single-axis or one-dimensional (1D) ultrasonic resonator, which consisted of a Langevin-type transducer (56 kHz) and a concave reflector, was used as a model example. Here, the 1D resonator was tuned to a distance between the horn and the reflector of $\sim 5\lambda/2$. Similar to the previous gas-flow imaging, the light source was operated in the continuous-wave (CW) mode, and the camera was not synchronized. In this asynchronous mode, the observed acoustic pressure field appeared static [Fig. 2(a)]. That is to say, the positions and pixel intensities of the positive and negative fringes [Fig. 2(a) blue and red regions] were not a function of time. One of the known uses of the static acoustic pressure field is to determine the quality factor (Q-factor) of an acoustic resonator, i.e. the maximum Q-factor can be found

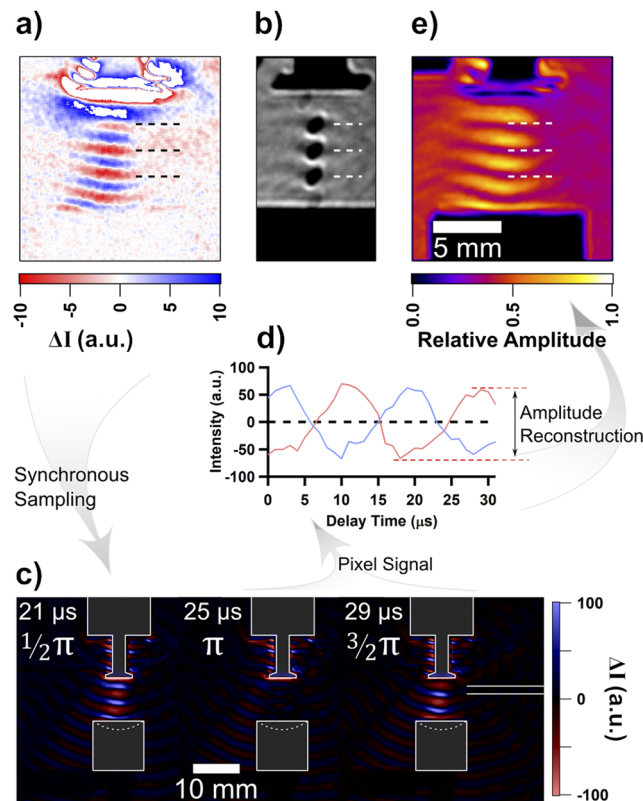


FIG. 2. Optical characterization of the one-dimensional acoustic resonator with DF-shadowgraphy. The background-subtracted acoustic pressure field is given in (a) from asynchronous-mode imaging. The nodes of the resulting resonant acoustic field are registered by water droplets (b) and marked by dashed lines in (a), (b), and (e). Defocusing-shadowgraphic images from synchronous-mode sampling are given in (c) and labeled with their corresponding delay time and phase angles. The transient pixel intensities of two example pixels are given in (d). The reconstructed amplitude distribution of the one-dimensional ultrasonic resonator is given in (e). The first and last rows of images are of different scaling factors.

when the distance between the horn (or transducer assembly) and the reflector is fully optimized. For an ultrasonic resonator designed for levitating liquid droplets, tuning the distance between the horn and the reflector (or the Q-factor) ultimately determines the shape of the droplet.³¹ In the example given here, the distance was empirically set to yield spherical levitated droplets with minimal vibrations and morphological distortions [Fig. 2(b)]. Moreover, the horn was used as a nebulizer to distribute water into the resonator, resulting in stable droplets at the nodes; this raw image [Fig. 2(b)] was used to label the pressure nodes where levitated objects experienced acoustic forces that counteract their gravitational pulls. Notably, the observed static acoustic pressure field appears to be asymmetric against the axial center of the horn, which is due to an off-axial alignment of the horn and the concave reflector.

In addition to the asynchronous mode, the driving signal for the ultrasonic transducer was used as the trigger source of a digital delay generator to control the light source [a blue light-emitting diode (LED), Fig. S2] by a $1\text{-}\mu\text{s}$ boxcar signal with variable delay to the transducer phase. Compared to that in the asynchronous

mode, the synchronization of the light source to the ultrasonic driver (synchronous mode) leads to more pronounced visibility of the transient acoustic field. Note that the camera parameter (i.e., exposure, gain, and frame rate) was carefully tuned so that the synchronous and asynchronous modes exhibited almost the same total light sensitivity. Meanwhile, the delay time sweep with respect to the trigger point allowed the measurement of transient intensities at individual pixels [Fig. 2(c)]. The ultrasonic transducer operated at ~ 56 kHz with our setup. Experimentally, we set a prescaling factor of 4 on the delay generator to record defocusing-shadowgraphic images for more than one full period corresponding to the acoustic frequency. For instance, three images are demonstrated here, representing the phase angles at $\pi/2$, π , and $3\pi/2$ [Fig. 2(c), from left to right]. In these transient images, both the leaked traveling wave and the standing wave inside the resonator volume can be seen. If each pixel is treated as an independent detector, the temporal pixel intensity can be obtained. For instance, the temporal intensities of two arbitrarily chosen pixels reveal acoustic pressure changes as a function in space [Fig. 2(d)]. Specifically, these two pixels were randomly chosen at the center of symmetry of the ultrasonic horn; their vertical heights are marked with white traces in the right panel of Fig. 2(c).

In terms of gaining the information for ultrasonic levitation from a force-analysis perspective, the amplitude change on the pixels, i.e., ΔI , is involved. The irrelevant phase information is disregarded here, whereas the amplitudes for each pixel were calculated by the difference in maximal and minimal pixel intensities [Fig. 2(d)]. Repeating this step programmatically for each pixel yields a spatial distribution that reflects the acoustic pressure field [Fig. 2(e)]; this operation is termed amplitude reconstruction. Referring to the levitated droplets [Fig. 2(b), dashed lines], the levitation spots are transferred and overlaid with the acoustic pressure distribution [Fig. 2(e), white-dashed lines]. As expected, the levitation positions agree with the determined nodes (zero acoustic amplitude). Moreover, based on the relationship between the acoustic force applied on a levitated object and the square of the acoustic

pressure,^{19,32} P_{ac}^2 , a vector field can be constructed on demand for further analysis (supplementary material, Sec. 3, Fig. S8).

SYNCHRONOUS-MODE ANALYSIS OF A TWO-DIMENSIONAL ACOUSTIC RESONATOR

The test with the 1D acoustic resonator implied a workflow for the characterization of a resonant acoustic field in general, which relies on synchronous-mode acquisition and the subsequent amplitude reconstruction. To test DF-shadowgraphy for more complicated scenarios, a simplified low-power two-dimensional (2D) acoustic resonator was built in-house with four ultrasonic speakers (TCT40-16) and assembled with a 3D-printed frame. Different from the 1D acoustic resonator, this 2D one can be operated in different modes [Fig. 3(b)]: (i) all four transducers are operated in the same phase or $\Delta\theta = 0^\circ$, and (ii) two transducers that face against each other form a pair, where the two pairs are driven in the reversed-phase mode, or $\Delta\theta = 180^\circ$. When all four transducers were driven in the same phase, the image sequence was recorded with DF-shadowgraphy [Fig. 3(a)]. Aside from the phases where the antinodes are clearly visible [Figs. 2(a), $\pi/2$ and $3\pi/2$], the transitions of the resonant acoustic field can be observed. Notably, the 2D acoustic resonator nearly produced a 2D standing wave inside the resonator volume, but slight imperfections are shown as well, such as the patterns at the phase angle, π . Specifically, the dimension of the frame or the distance between two opposite transducers was calculated based on an ideal sound speed in the air of 340 m/s, which varies depending on the laboratory conditions and location. The results demonstrate the capability and applicability of the defocusing-shadowgraphy method for acoustic resonator diagnoses.

Once the temporal image series were recorded, the amplitude map when all transducers were operated in the same phase can be reconstructed [Fig. 3(c), experimental]. Compared to the phase-domain simulation of the 2D resonator with COMSOL (v 5.3), the agreement between the experimentally determined acoustic pressure field and the simulated one can be readily seen. Despite the

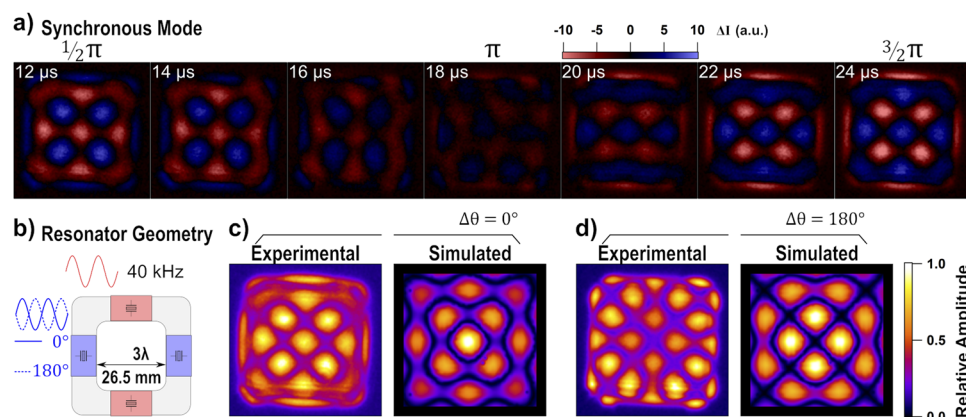


FIG. 3. Optical characterization of the 2D acoustic resonator with DF-shadowgraphy. The image sequence for the transient acoustic field is given in (a) according to the trigger delay time; the images are labeled with their phase angles. The geometry of the 2D acoustic resonator is given in (b). The transducer pairs are color-coded in red and blue. The amplitude-reconstructed acoustic field for the same phase and the reversed-phase is given in (c)-experimental and (d)-experimental. The simulated amplitude maps for both configurations are given in (c) and (d), respectively.

differences in absolute intensities that reflect the antinodes, the spatial patterns and center symmetry are nearly identical between the experimental and the simulated results. Similarly, the same workflow was applied to the case where the two pairs of transducers were operated 180° out-of-phase [Fig. 3(d), experimental], which agreed with the simulated result [Fig. 3(d), simulated] as well.

Notably, the images of acoustic resonators in the two examples were used as-is to reconstruct the spatial acoustic pressure distributions. Contradictorily, the gas-stream example suggested that DF-shadowgraphy projected the IoR distribution with both positive and negative components, where the true IoR distribution can only be unipolar. That is to say, an inversion from the image back to the IoR gradient is necessary to interpret the spatial features of a gas stream. However, the images of resonant acoustic fields from DF-shadowgraphy appeared to directly reflect the pressure gradients without any distortion, different from a gas stream. To understand the nature of the defocusing-shadowgraphy method and justify the validity of this method for characterizing resonant acoustic fields, we approach the fundamentals from a theoretical perspective.

THEORETICAL APPROXIMATION

With the DF approach shown in this work, which involves a lens combination (Fig. 1, FL), the formulation of images that represents the patterns of IoR in space became more sophisticated than parallel-light shadowgraphy or that with converging/diverging light. Thus, instead of interpreting the recorded images with ray-tracing theory, we approach the underlying principle for image formation through the Fourier-optics theoretical framework. For clarity, the dimension along the travel direction of the light is defined as the z-axis; the plane parallel to the mirror, i.e. the sampling plane, is defined as the x-y plane. The wavefront, $U(x, y)$, can be expressed in combination with Snell's law [supplementary material, Sec. 4, Eqs. (S4) and (S5)]. The phase perturbation due to the difference in refractive indices between the room air and the sample can be given by

$$\phi(x, y) = \int \frac{2\pi}{\lambda} (n_s(x, y) - n_{air}) dz, \quad (1)$$

where λ is the wavelength of the illumination light, $n_s(x, y)$ is the effective refractive index of the sample distributed in the x-y plane, n_{air} is the refractive index of the room air, and z is the optical depth. The wavefront can then be expressed by the multiplication of the amplitude by the exponential of the imaginary phase perturbation, $i\phi(x, y)$ (supplementary material, Sec. 4). Note that this phase perturbation is not directly visible with a camera. In schlieren imaging, the wavefront is focused onto the Fourier transform plane, at which spatial filters (e.g., a knife-edge) are placed. The spatial filter modulates the wavefront and produces visible schlieren patterns on the final imaging plane. In our case, the defocusing operation served to modulate the wavefront instead of spatial filters.

The optical system consists of a parabolic mirror that converged the light to its focal point at its $2f$ distance; the divergent light was then recollimated with the focusing lens combination that contained two spherical plano-convex lenses. The simple optical geometry resulted in a complicated impulse response function or otherwise

known as the point spread function. Instead of expressing all the terms involved in our optical geometry, a simplified formula can be given by the convolution relation,

$$I(\tilde{x}, \tilde{y}) = \kappa |h(x, y; d) \otimes U(x, y)|^2, \quad (2)$$

where $I(\tilde{x}, \tilde{y})$ is the intensity distribution of the image on the detector, which is the absolute square of the wavefront in the case of incoherent light; \tilde{x} refers to the pixel coordinate containing a magnification factor [Eq. (S8)]; κ is the intensity correction factor; $h(x, y; d)$ is the overall impulse response function that includes all three optics at a specific defocusing distance, d ; and \otimes is the convolution symbol. More specifically, a kernel of an impulse response function was manually chosen to reflect the optical system, which is given by

$$h(x, y; \sigma) = G(x, y; \sigma) \otimes T_{obj}(x, y), \quad (3)$$

$$T_{obj} = \frac{2\pi}{\lambda} (n_{BK-7} - n_{air}) (\delta_{sphere} - \delta_{parabola}), \quad (4)$$

where $G(x, y; \sigma)$ is a Gaussian term to mimic the image blurriness due to defocusing and T_{obj} is the objective function where δ is the lens geometry. Note that we included two terms of δ here, where δ_{sphere} and $\delta_{parabola}$ represent the spherical lens (i.e. the

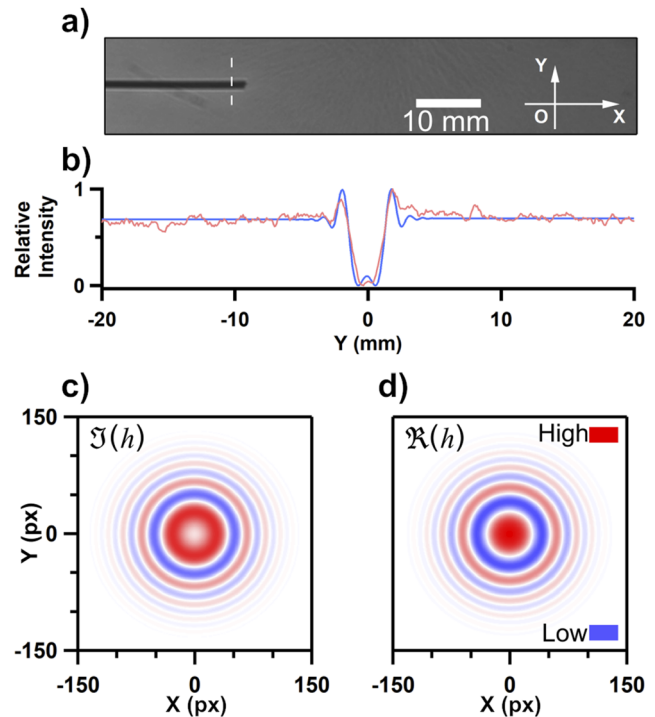


FIG. 4. Finding the numerical expression of the impulse response function. A background image at a defocusing distance, $d = 2$ mm, is given in (a). The dashed white line in (a) represents the slice, which is given in (b) with the solid-red trace. The truncated 1D impulse response function is shown in (b) (solid blue trace). The 2D impulse response function is presented by the imaginary and real parts in (c) and (d), respectively.

focal lenses) and the residual contributions from the parabolic mirror, respectively. The impulse response function of the optical system, $h(x, y;)$, can be calculated solely relying upon precise measurements of all parameters of the optical components (including refractive indices of air and lenses). In a more practical sense, we exploited the information that is already encoded in experimental images to approximate the numerical expression of h in the form of a matrix. The setup of the impulse response function simplifies the experimental configuration to a monochromatic light source (supplementary material, Sec. 4). Meanwhile, the initial phase perturbation from a non-coherent light source is omitted here for simplicity. More toward a practical sense, the equation set is more of an empirical model that can be used to interpret the experimental observations.

To obtain the numerical impulse response function, the capillary itself can be used as a target of known dimensions to calculate the matrix at a certain \bar{d} . Practically, a vertical slice (or y -slice) was manually picked on the projection of the gas-outlet capillary [Fig. 4(a), white-dashed line]. The consequent 1D slice [Fig. 4(b), solid-red trace] was used to tune the parameters of $h(y)$ in a plane [Fig. 4(b), solid blue trace] with a global optimization method (based on the Nelder–Mead simplex method).³³ Overall, the representative parameters are the width of the Gaussian blur, σ ; the radius of the equivalent spherical lens, R ; the focal length of the parabolic residue, f ; a conversion factor that describes the dimensional relation in length from the image plane to the detector surface in the unit of (mm/px), C_F ; and the intensity correction factor, κ (Table S1). Consequently, the numerical expression of h in the form of a matrix can be obtained [Figs. 4(c) and 4(d)].

NUMERICAL SIMULATION AND POTENTIAL OF QUANTITATIVE MEASUREMENTS

The numerical solution of the impulse response function principally contains all information of the optical system. However, the inversion of a recorded image back into the true phase image, or IoR distribution, turns into an ill-posed inverse problem and cannot be simply achieved by deconvolution. While an image is recorded, the phase information is lost, represented by the absolute operation in Eq. (2). That is to say, it is impossible to differentiate absorption and phase distortion from a defocusing-shadowgraphy image unless additional information along an orthogonal dimension is included (e.g., wavelength and/or \bar{d}). Fortunately, the known experimental parameters allow forward simulations (in contrast to inversion) from a given IoR gradient to an expected image [Figs. 5(a) and 5(b)]. Based on the experimental results [Fig. 5(a)], an image for flowing gases can be simulated with two segments representing the capillary and gas stream: a phase-independent part reducing the amplitude of the light due to the capillary blockage [Eq. (1), Fig. S10(a)] and the other part that does not affect the amplitude but represents the impact of the IoR field of the gas stream on the phase [Fig. S10(b)]. For the simulation, a complex wavefront matrix that combines the segments of the capillary and gas stream can be assigned corresponding to the experimental condition (supplementary material, Sec. 5). The convolution of the wavefront, U , with the determined impulse response function, h , yields a simulated image [Fig. 5(b)], which resembles the features exhibited in experimental results.

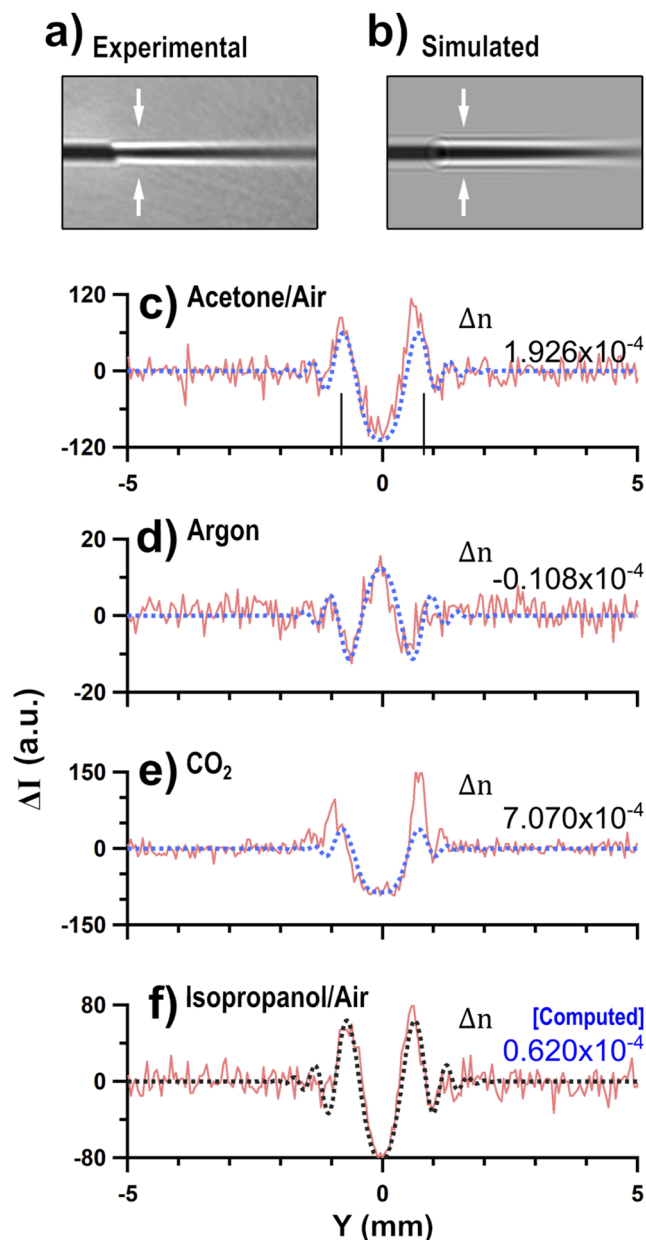


FIG. 5. Experimental and simulated images of a gas stream with a different refractive index compared to the room air. The experimental and simulated images of the isopropanol/air mixture are given in (a) and (b), respectively. The white arrows in (a) and (b) indicate the positions of the section views. The section views of the acetone/air mixture, pure argon, pure CO₂, and the isopropanol/air mixture are given in (c)–(f), respectively. The solid-red traces are the experimental section views; the dashed blue and black traces are simulated.

Importantly, the numerical matrix of the impulse response function was optimized by parameters that reflect values with physical meanings in accordance with the experimental condition (e.g., wavelength, refractive indices of the sample gas and air, etc.).

Meanwhile, the gas stream was mimicked by the projection of a cylinder with a radius of the inner diameter of the capillary [Fig. S12(a)]. Subsequently, the phase perturbations were calculated based on known refractive indices of various gases and integrated along the z -direction. Because we did not include any fluid dynamic simulations, the expansion of the gas stream was merely described empirically [supplementary material, Sec. 5, Fig. S12(b)]. For improved accuracies, we arbitrarily selected a slice coordinate that is close to the capillary outlet [Figs. 5(a) and 5(b), white arrows, 50 px or ~ 2.5 mm]. The use of true experimental parameters allowed accurate representations of the observation through computations [Figs. 5(c)–5(f)]. One special case is when CO_2 was used as a model sample. Under our experimental condition, the phase perturbation ϕ of CO_2 at the center of steam was slightly over 2π . Thus, the consequent slice of CO_2 exhibits a flat region near the $Y = 0$ mm point, unlike the other examples demonstrated here. Moreover, the simulated slice of CO_2 mostly agreed with experimental observations, especially in terms of the shape. The major inaccuracies are found at the edges of the flow, which can be attributed to the inherent errors from the flow approximations without true fluid dynamic consideration.

Two out of the four examples [Figs. 5(c)–5(f)] revealed the quantitative potential of the defocusing-shadowgraphy method, which are the acetone and isopropanol vapors carried by air [Figs. 5(c) and 5(f)]. The refractive index of acetone vapor was calculated based on the known IoR of pure acetone vapor and its vapor pressure at 20°C . The resulting IoR of the air/acetone mixture, $n_{\text{acetone}} - n_{\text{air}}$, was 1.926×10^{-4} . Agreement is found in both the shape of the projection and observed pixel intensities for this example [Fig. 5(c)]. Similarly, an attempt was made to estimate the IoR of isopropanol vapor, which is not readily available in common databases. That is to say, even with the vapor pressure of isopropanol, it was not possible to calculate the IoR of the isopropanol/air mixture (unlike the acetone example). Through the experimentally determined slice [Fig. 5(f), solid-red trace] and the known impulse response function, h , the refractive index of the isopropanol/air mixture can be determined as $\Delta n = 0.620 \times 10^{-4}$ through optimizing the phase perturbation [Fig. 5(f), dashed-black trace]. This example case of IoR determination implies that the defocusing method demonstrated in this study can be used as a means for absolute IoR measurements.

Relying on the agreement between the experimental results and the simulated images, this method, DF-shadowgraphy, is much closer to phase-imaging techniques than conventional shadowgraphy without the need for coherent or partially coherent light,³⁴ spatial filters,^{6,35} or interferometers.^{6,36} We propose that the capability of visualizing the phase information semi-quantitatively is due to the asymmetry in the reflection mirror and focusing lens or, namely, the difference between spherical and parabolic surfaces. In contrast to a common $4f$ -Fourier optical setup, where conjugate lenses are used, our optical path contains a “flaw,” which is the residual term in the lens function [Eq. (4)] caused by the sum of all remaining aberrations. Modern lenses are designed to correct chromatic and spherical aberrations. However, a “perfectly” designed commercial lens can be closer to a parabola, which results in a very small residue of the lens function. Experimentally, commercial lenses could not produce images as sensitive as our experimental observations (data not shown). In contradiction, the low-cost spherical lenses greatly

benefit the phase-visualization purpose as demonstrated in this work.

FROM A PRACTICAL PERSPECTIVE

As demonstrated by the gas flow compared to the knife-edge schlieren method, the DF-shadowgraphy approach introduced in this work appeared to be quite sensitive close to the outlet capillary but less sensitive in the sense of showing the flow features when the gas stream traveled further. Through the theoretical investigation, the fundamental reason can be attributed to the inherent non-linearity of the impulse response function, h . Very similar to background removal methods based on wavelet transforms, the convolution kernel (h , in this case) removes nearly constant backgrounds; contrastingly, localized features are emphasized. Even though we did not quantitatively determine the range of applicability of this defocusing method, it can be expected that the approach described in this work may exhibit certain limitations: spatial features across a large range (e.g., significantly greater than the span of h) may be undetectable.

Fortunately, the measurements of acoustic fields suggested otherwise. The distance between two adjacent nodes of an acoustic standing wave is defined by the resonance frequency of the transducer assembly. Based on our experimental results at 40 and 56 kHz, we would consider that our current optical geometry can be used to map acoustic fields in the frequency range of 20–80 kHz without inversion (supplementary material, Sec. 6). Another aspect of the acoustic field different from a gas stream is that the spatial features primarily consist of sinusoidal components. Based on the numerical expression of the impulse response function, h , further simulations suggested that the convolution [Eq. (4)] does not clutter the visualization of acoustic fields (supplementary material, Sec. 6, Fig. S14). That is to say, for acoustic field measurements, at least for those that operate at a single frequency, inversion can be obviated, that is, this DF-shadowgraphy method can be considered a “what you see is what you get” approach for acoustic field mapping.

The only adjustable parameter in the physical setup is the defocusing distance, d . Simply from the boundary conditions, i.e. at focus and infinitely far from focus, the expected images should be sharp but do not include any phase information and infinitely blurred so that no spatial feature can be distinguished, respectively. Thus, an optimized d is expected in between, at which the image is blurred to a state that the phase-induced spatial patterns can still be recognized. In this work, d was experimentally found. The selected $d = 2$ mm was later found to be at nearly maximum sensitivity with acceptable blurriness of the image (Fig. S16, supplementary material, Sec. 7). The corresponding loss in lateral resolution is minute and tolerable especially since this blurring scales with the system’s optical magnification factor, while high-resolution detectors are readily available.

CONCLUSION

Throughout this work, we demonstrated a simple optical method, termed DF-shadowgraphy, to obtain images that reflect the lateral IoR distributions. With the support of a mathematical description, the impulse response function of a specific setup can be readily determined; the numerical solution of this transfer

function can be potentially used for absolute IoR determination. While further studies and tests are still needed to prove the validity of DF-shadowgraphy, the results with simple gas streams and more sophisticated resonant acoustic fields already indicated that DF-shadowgraphy can serve as an alternative for schlieren imaging, overcoming the most common shortcomings of schlieren, i.e. the anisotropic sensitivity, which is introduced by the knife blade axis and its non-quantitative character.

Because of the complexity of the impulse response function, h , the inversion from images back to the true distribution of refractive indices can be difficult. However, for sample systems where the convolution does not alter the image representation of the spatial features, the inversion can be completely obviated. Furthermore, for the improved representation of an acoustic field, the concept of amplitude reconstruction was introduced. In the sense that the ambient object manipulations are of interest, the amplitude reconstruction workflow can be very convenient. Moreover, the agreement between the experimentally determined acoustic amplitude distribution compared to numerical simulation supported the validity of the DF-shadowgraphy method.

In contrast to the anticipation of expensive and specialized optical components, the DF-shadowgraphy method used the “defect” in the optical path, which is the asymmetry of the parabolic mirror and spherical lens; both are readily available on the market and at very low costs. The results of selecting these non-ideal optical components, interestingly, resembled a complex wave filter, which gains unexpected advantages such as imaging capabilities for mapping the distribution of IoR under ambient conditions.

EXPERIMENTAL

The single-mirror coincident optical geometry is given in Fig. 1(a). The optical components are given, following the light path. A three-color light-emitting diode (LED) was used only in the blue mode (supplementary material, Sec. 1, Fig. S2). In either the continuous-wave (CW) mode or the pulsed mode (for synchronous-mode measurements), the LED was operated under the current-controlled mode without a feedback loop (Fig. S3). The light from the LED was sent through a pin-hole made in-house at a diameter of $\sim 500\ \mu\text{m}$. A neutral-density 50/50 beam splitter plate (unknown manufacture, recycled) was placed along the optical path to guide the reflected light from the mirror. An aluminum-coated parabolic mirror ($f = 1200\ \text{mm}$) was used. The distance and the relative position between the light source and the mirror were tuned to which the reflected image of the pin-hole perfectly aligned with itself. The beam splitter reflected half of the converging beam from the mirror toward the focusing lens, where two plano-convex lenses ($f = 175$ and $f = 125\ \text{mm}$, N-BK7 uncoated, Thorlabs, Dachau, Germany) were assembled with a gap of $\sim 5\ \text{mm}$. A monochrome camera (EO5012M, Edmund Optics, Barrington, NJ, USA) was used to record all experimental images. Throughout this work, the camera was operated in the software-trigger mode; synchronous-mode measurements were achieved by pulsing the LED, yielding stroboscopic projections. The camera control and its readout were controlled with software made in-house through the Edmund uEye application development interface (API). The gain was set to 50 (manufacture unit) for all cases; the exposure time for asynchronous and synchronous modes was set to 200 and 500 ms, respectively.

All chemicals used in this study were of analytical grade. Isopropanol and acetone were purchased from Sigma-Aldrich, Germany. House-supplied argon was used. CO_2 was made in-house through the Na_2CO_3 and citric acid aqueous reaction. The schematic of gas introduction can be found in the supplementary material, Sec. 1, Fig. S1. The gas flow rate was controlled manually without a feedback loop. The flow patterns for each case were manually adjusted to which laminar flow patterns near the outlet capillary were observed.

Two ultrasonic resonators were used in this work. The 1D ultrasonic levitator was commercially available (Levitator, Tec5 A.G., Steinbach, Germany), operating at $\sim 56\ \text{kHz}$. The 2D ultrasonic resonator was built in-house. The driver circuit schematic is given in Fig. S4. The transducers (TCT40-16) were operated at $\sim 40\ V_{\text{p-p}}$ in all cases.

The synchronous-mode measurements were achieved by pulsing the LED through a homemade driver board (schematic can be found in Fig. S3). The LED received trigger signals from a digital delay generator (DG-645, Stanford Research Systems, Sunnyvale, CA, USA), configured to the external trigger mode for synchronous acquisition. Note that for the frequency range of several tens of kHz, the digital delay generator was excessive; it can be replaced by a microcontroller (e.g., Cortex M4) for the used temporal resolution of $1\ \mu\text{s}$, which lowers the overall cost of the platform.

Numerical simulations of the acoustic field were performed with COMSOL (v.5.3). The phase-domain 2D pressure-acoustic study was used to generate the simulated images of Figs. 3(c) and 3(d). The initial sound pressure was set to 10 Pa manually. The default medium properties (air) were used as-is.

SUPPLEMENTARY MATERIAL

The supplementary material is available free of charge on the publisher website: Sec. 1: extended experimental information; Sec. 2: additional data for gas stream visualization; Sec. 3: additional data for acoustic resonators; Sec. 4: extended theoretical approximation; Sec. 5: gas-stream simulation; Sec. 6: justification for acoustic field mapping; Sec. 7: impulse response as a function of \bar{d} ; the supplementary material includes Figs. S1–S16.

ACKNOWLEDGMENTS

The authors would like to acknowledge our funding agency, Deutsche Forschungsgemeinschaft (DFG, Grant No. 351360803), for the financial support of this work.

The authors appreciate the assistance by Dr. Rainer Krankenhagen from BAM F.B. 8.7 for COMSOL access.

AUTHOR DECLARATIONS

Conflict of Interest

The authors have no conflicts to disclose.

DATA AVAILABILITY

The data that support the findings of this study are available from the corresponding author upon reasonable request.

REFERENCES

- ¹G. S. Settles, *Schlieren and Shadowgraph Techniques: Visualizing Phenomena in Transparent Media* (Springer Science & Business Media, 2001).
- ²G. S. Settles and M. J. Hargather, "A review of recent developments in schlieren and shadowgraph techniques," *Meas. Sci. Technol.* **28**, 042001 (2017).
- ³L. A. Vasil'ev, *Schlieren Methods* (Israel Program, 1971).
- ⁴H. Richard and M. Raffel, "Principle and applications of the background oriented schlieren (BOS) method," *Meas. Sci. Technol.* **12**, 1576 (2001).
- ⁵G. Meier, "Computerized background-oriented schlieren," *Exp. Fluids* **33**, 181–187 (2002).
- ⁶L. Joannes, F. Dubois, and J.-C. Legros, "Phase-shifting schlieren: High-resolution quantitative schlieren that uses the phase-shifting technique principle," *Appl. Opt.* **42**, 5046–5053 (2003).
- ⁷G. E. Elsinga, B. W. Van Oudheusden, F. Scarano, and D. W. Watt, "Assessment and application of quantitative schlieren methods: Calibrated color schlieren and background oriented schlieren," *Exp. Fluids* **36**, 309–325 (2004).
- ⁸M. J. Hargather and G. S. Settles, "A comparison of three quantitative schlieren techniques," *Opt. Lasers Eng.* **50**, 8–17 (2012).
- ⁹M. A. B. Andrade, N. Pérez, and J. C. Adamowski, "Review of progress in acoustic levitation," *Braz. J. Phys.* **48**, 190–213 (2018).
- ¹⁰E. A. Crawford, C. Esen, and D. A. Volmer, "Real time monitoring of containerless microreactions in acoustically levitated droplets via ambient ionization mass spectrometry," *Anal. Chem.* **88**, 8396–8403 (2016).
- ¹¹F. Delißen, J. Leiterer, R. Bienert, F. Emmerling, and A. F. Thünemann, "Agglomeration of proteins in acoustically levitated droplets," *Anal. Bioanal. Chem.* **392**, 161–165 (2008).
- ¹²H.-L. Cao *et al.*, "Rapid crystallization from acoustically levitated droplets," *J. Acoust. Soc. Am.* **131**, 3164–3172 (2012).
- ¹³S. E. Wolf, J. Leiterer, M. Kappl, F. Emmerling, and W. Tremel, "Early homogeneous amorphous precursor stages of calcium carbonate and subsequent crystal growth in levitated droplets," *J. Am. Chem. Soc.* **130**, 12342–12347 (2008).
- ¹⁴A. Stindt, M. Albrecht, U. Panne, and J. Riedel, "CO₂ laser ionization of acoustically levitated droplets," *Anal. Bioanal. Chem.* **405**, 7005–7010 (2013).
- ¹⁵C. Warschat, A. Stindt, U. Panne, and J. Riedel, "Mass spectrometry of levitated droplets by thermally unconfined infrared-laser desorption," *Anal. Chem.* **87**, 8323–8327 (2015).
- ¹⁶A. Bierstedt, C. Warschat, Y. You, K. Rurack, and J. Riedel, "Stimulated Raman scattering by intracavity mixing of nanosecond laser excitation and fluorescence in acoustically levitated droplets," *Anal. Methods* **12**, 5046–5054 (2020).
- ¹⁷L. Cox, A. Croxford, B. W. Drinkwater, and A. Marzo, "Acoustic lock: Position and orientation trapping of non-spherical sub-wavelength particles in mid-air using a single-axis acoustic levitator," *Appl. Phys. Lett.* **113**, 054101 (2018).
- ¹⁸A. Marzo *et al.*, "Realization of compact tractor beams using acoustic delay-lines," *Appl. Phys. Lett.* **110**, 014102 (2017).
- ¹⁹S. Baer *et al.*, "Analysis of the particle stability in a new designed ultrasonic levitation device," *Rev. Sci. Instrum.* **82**, 105111 (2011).
- ²⁰A. Stindt *et al.*, "Experimental and numerical characterization of the sound pressure in standing wave acoustic levitators," *Rev. Sci. Instrum.* **85**, 015110 (2014).
- ²¹M. Brown, M. Safsamghabadi, D. Sanford, and C. Schaal, "Shadowgraph visualization of the scattering of focused ultrasonic waves at bone-like constructs," *Exp. Mech.* **60**, 861–872 (2020).
- ²²K. Hasegawa, A. Watanabe, A. Kaneko, and Y. Abe, "Coalescence dynamics of acoustically levitated droplets," *Micromachines* **11**, 343 (2020).
- ²³S. Zhao and J. Wallaschek, "A standing wave acoustic levitation system for large planar objects," *Arch. Appl. Mech.* **81**, 123–139 (2011).
- ²⁴N. Kudo, "A simple technique for visualizing ultrasound fields without schlieren optics," *Ultrasound Med. Biol.* **41**, 2071–2081 (2015).
- ²⁵M. Biss, G. Settles, M. Hargather, L. Dodson, and J. Miller, *Shock Waves* (Springer, 2009), pp. 91–96.
- ²⁶A. Ozcan and E. McLeod, "Lensless imaging and sensing," *Annu. Rev. Biomed. Eng.* **18**, 77–102 (2016).
- ²⁷M. Legrand, A. Lecuona, J. Nogueira, and R. Forte, in 17th International symposium on Applications of Laser Techniques to Fluid Mechanics, Lisbon, Portugal, July 7–10, 2014.
- ²⁸T. W. Fahringer and B. S. Thurow, "Filtered refocusing: A volumetric reconstruction algorithm for plenoptic-PIV," *Meas. Sci. Technol.* **27**, 094005 (2016).
- ²⁹A. Bierstedt, U. Panne, and J. Riedel, "Confinement and enhancement of an airborne atmospheric laser-induced plasma using an ultrasonic acoustic resonator," *J. Anal. At. Spectrom.* **33**, 135–140 (2018).
- ³⁰R. K. Tyson, *Principles and Applications of Fourier Optics* (IOP Publishing, Bristol, UK, 2014).
- ³¹A. L. Yarin, M. Pfaffenlehner, and C. Tropea, "On the acoustic levitation of droplets," *J. Fluid Mech.* **356**, 65–91 (1998).
- ³²P. J. Westervelt, "Acoustic radiation pressure," *J. Acoust. Soc. Am.* **29**, 26–29 (1957).
- ³³J. C. Lagarias, B. Poonen, and M. H. Wright, "Convergence of the restricted Nelder–Mead algorithm in two dimensions," *SIAM J. Opt.* **22**, 501–532 (2012).
- ³⁴D. Paganin and K. A. Nugent, "Noninterferometric phase imaging with partially coherent light," *Phys. Rev. Lett.* **80**, 2586 (1998).
- ³⁵A. Shanker, L. Tian, and L. Waller, in *Three-Dimensional and Multidimensional Microscopy: Image Acquisition and Processing XXI* (International Society for Optics and Photonics, 2016), No. 89490R.
- ³⁶M. Mir, B. Bhaduri, R. Wang, R. Zhu, and G. Popescu, "Quantitative phase imaging," *Prog. Opt.* **57**, 133 (2012).